Construction and Building Materials 223 (2019) 554–565

Contents lists available at ScienceDirect

Construction and Building Materials

journal homepage: www.elsevier.com/locate/conbuildmat

Direct synthesis of a solid calcium-silicate-hydrate (C-S-H)

Riccardo Maddalena [a,b,*], Kefei Li [c], Philip A. Chater [d], Stefan Michalik [d], Andrea Hamilton [b,*]

[a] Cardiff University, School of Engineering, Cardiff CF24 3AA, UK
[b] University of Strathclyde, Department of Civil and Environmental Engineering, Glasgow G1 1XJ, UK
[c] Tsinghua University, Department of Civil Engineering, 100084 Beijing, PR China
[d] Diamond Light Source Ltd., Harwell Science and Innovation Campus, Didcot, Oxfordshire OX11 0DE, UK

HIGHLIGHTS

- Solid synthetic C-S-H is produced from calcium hydroxide and nano-silica.
- Shown to be crystallographically similar to the more commonly produced slurry.
- Curing time studies show significant C-S-H is produced after 1 day for C/S ratio = 0.81.

ARTICLE INFO

Article history:
Received 19 December 2017
Received in revised form 30 May 2019
Accepted 3 June 2019
Available online xxxx

Keywords:
Calcium-silicate-hydrate (C-S-H)
Characterization
Thermal analysis
X-ray diffraction

ABSTRACT

We present new results on solid (monolithic) synthetic C-S-H made at room temperature from easily obtainable calcium sources (calcium oxide, calcium hydroxide) and nanosilica (w/s = 2) with a 2 minute mixing time. Using synchrotron X-ray diffraction combined with TGA/DSC, ^{29}Si NMR and synchrotron pair distribution function (PDF) data we show that the solid C-S-H is crystallographically similar to the more conventionally made synthetic C-S-H slurry. We show that C-S-H is present after 1 day curing (C/S = 0.81) and no X-ray visible portlandite is present from day 3. PDF data shows that the ordered domain size is 2.5 – 4.5 nm, depending on the fit chosen.

1. Introduction

Cement is the world's most produced material with nearly 2 billion tonnes manufactured globally per year, which creates 1.6 billion tonnes of CO_2 and makes cement production a significant contributor to greenhouse gas emissions [1]. Calcium silicate hydrate (C-S-H) gel, a poorly crystalline phase with variable stoichiometry, makes up *ca.* 75% wt. of the final hydrated product in ordinary Portland cement (OPC) [2], therefore the bulk and micro-structural properties of C-S-H gel have attracted significant research activity over the last few decades, particularly its ability to adsorb contaminants and radionuclides such as Cl, Cs, Zn, Sr, Co, U etc. [3–5].

To accurately characterise and structurally tailor C-S-H, researchers have attempted to synthesize pure C-S-H without any accessory minerals present. This has been carried out in a variety of ways with differing degrees of complexity. Early work on synthetic C-S-H from Cong and Kirkpatrick (1996) synthesized C-S-H from β-C_2S and water or from fumed silica, lime and water at final calcium to silica (C/S) molar ratios of 0.4–1.85 through a long-term reaction process, lasting 2–10 months [6]. Samples were dried under nitrogen flow and characterized using laboratory powder X-ray diffraction (XRD), ^{29}Si MAS NMR spectroscopy and X-ray fluorescence (XRF). Harris et al. (2002) synthesized C-S-H by mixing calcium oxide and colloidal silica suspension under a nitrogen atmosphere, to obtain an entire sample C/S ratio range of 0.8–3.0. The actual C/S ratio of the C-S-H in the composite C-S-H and CH system obtained at higher target C/S values is unknown because it was not measured [7]. Their C-S-H obtained although made with a low H_2O/CaO ratio of 2,was probably not a 3D solid, and was used for extended leaching tests with no solid state chemical or mechanical characterization performed. Chen et al. (2004) [2] made synthetic C-S-H using the 'double decomposition' technique which involves precipitating C-S-H from dissolved sodium silicate added to dissolved calcium nitrate but their focus was also C-S-H solubility. C-S-H at low C/S ratio can be synthesised from calcium

* Corresponding authors.
E-mail addresses: maddalenar@cardiff.ac.uk (R. Maddalena), andrea.hamilton@strath.ac.uk (A. Hamilton).

https://doi.org/10.1016/j.conbuildmat.2019.06.024
0950-0618/

hydroxide and microsilica in liquid suspension with a mixture of comb polymers and phosphated polycondensate, as reported in the patent US 2011/0269875 A1 [8]. Nanocomposites of C-S-H and comb-like copolymers were synthesised by a rapid co-precipitation method from aqueous calcium carbonate and sodium silicate solution at a fixed C/S = 1.0 [9]. Tränkle et al. (2013) obtained 11 Å tobermorite by microwave assisted synthesis using quartz as the Si precursor with silicic acid and calcium hydroxide at low C/S molar ratios (0.36–0.83) [10]. TEM analysis showed the formation of nano-crystalline C-S-H but despite the high degree of crystallinity obtained, some unreacted material remained. Recent research has produced pure synthetic C-S-H with a high C/S ratio of 2, and no accessory portlandite, for the first time, by reacting aqueous calcium nitrate and sodium silicate at constant pH and under conditions of high supersaturation [11]. The C/S ratio is known to play a crucial role in the formation of C-S-H and influences not only the chemistry but also the compressive strength [12].

The simplest precipitation technique is to combine reactive silica with Ca (either CaO or $Ca(OH)_2$) and while this method has been used before to make C-S-H [13,6,14–19], the C-S-H was produced by using a high water to solid ratio of *ca.* w/s = 3–8+ which produced a slurry that was filtered or was mechanically milled then filtered [14–16]. In this work we produce solid C-S-H, which simply mixes calcium hydroxide with nano-silica and deionised water, at fixed water content (w/s = 2) and room temperature without microwave assistance or applied heat, and with mixing time of a few minutes. In addition, the C-S-H is solid state, which has a potential range of uses in construction and environmental contaminant remediation, which a slurry may not have. The novelty of this technique is its relative simplicity, speed, comparative low cost and formation of solid C-S-H which can be designed and characterised both mechanically and physico-chemically.

Table 1
Characterisation of calcium hydroxide and nano-silica solution from the data sheet provided by the supplier.

Material	Calcium hydroxide	Nano-silica
Physical state	White fine powder	Suspension in H_2O
Composition	$Ca(OH)_2$: ⩾95.0%	SiO_2: ⩾50.0%
	S compounds: ⩽0.1%	H_2O: ⩾50.0%
	$CaCO_3$: ⩽3.0%	
Anion traces	Cl^- :⩽0.03%	Cl^- :⩽0.05%
Cation traces	Fe: ⩽0.05%	
	K: ⩽0.05%	
	Mg: ⩽0.05%	
	Na: ⩽0.05%	
	Sr: ⩽0.05%	
pH at 25 °C	12.4 (slurry)	8.5–9.5
Particle size range (nm)	–	5–20
Mass density at 25 °C (g cm^{-3})	2.24	1.40
Specific area (m^2 g^{-1})	20–41 (hydrated)	110–150

2. Materials and methods

2.1. Materials

Synthetic C-S-H phases were prepared using calcium hydroxide or calcium oxide and nano-silica, at set target C/S molar ratios. Reagent grade powdered calcium hydroxide, $Ca(OH)_2$, (molecular mass: 74.093 g mol^{-1}) commercially available from Sigma Aldrich was used. Calcium oxide was obtained by controlled calcination of reagent grade calcium carbonate. Ludox TM-50 nano-SiO_2 (molecular mass: 60.08 g mol^{-1}) aqueous suspension was also purchased from Sigma Aldrich. Nano-silica particle size range is 5–20 nm. Decarbonated water was used for mixing, made by bubbling nitrogen through deionised water [6]. Component material characteristics are reported in Table 1.

2.2. Synthesis process

Synthetic C-S-H phases were prepared according to the target C/S molar ratios in Table 2 at room temperature. Dry calcium hydroxide or calcium oxide powder was manually mixed with nano-silica suspension for two minutes at water to total solid ratio (w/s) = 2. Due to the large specific surface area of the nano-silica, a high water content is needed to allow homogeneous mixing. Although a target C/S = 2.4 is given for the final sample in the series, the aim was not to make a pure C-S-H phase material with so high a C/S ratio, but to provide an excess of calcium and to use TGA to estimate the actual C/S ratio. After mixing under a nitrogen atmosphere to minimize carbonation, samples were cast into plastic moulds (2.5 × 2.5 × 2.5 cm), stored in a sealed nitrogen environment at controlled conditions (20 ± 1 °C, 95 ± 1% relative humidity) and cured for a maximum of 28 days. Bleeding or phase segregation of the paste was not observed. After curing for 1, 3, 7 or 28 days, samples were placed in an acetone bath for 24 h to remove pore water and halt the hydration for accurate materials characterisation [20,21] then dried under constant nitrogen flow for an additional 24 h. Specimens were then stored in a vacuum-sealed bag until required. A schematic process of the synthesis is shown in Fig. 1. Samples for TGA/DSC analysis alone were oven dried at 60 °C for 100 h to remove pore water prior to TGA analysis. All samples were then manually ground and sieved, to obtain a homogeneous fine powder for TGA and XRD characterisation.

2.3. Thermo-gravimetric analysis

Thermo-gravimetric (TG) and differential scanning calorimetry (DSC) data were collected using a NETSZCH STA 449 F1 Jupiter. Measurements were conducted on powder samples weighing 15–25 mg, under constant nitrogen flow at a heating rate of 10 °C min^{-1} from 25 °C to 1000 °C. Prior to measuring, samples were oven-dried at 60 °C for *ca.* 100 h under nitrogen flow to remove any remaining pore water and acetone [16]. Results are

Table 2
Sample mixes, C/S target ratio values, curing time per sample, and mixing proportion for 100 g of solid calcium hydroxide + nano-silica.

Sample ID	Target C/S ratio mol/mol	Curing time days	$Ca(OH)_2$ g	SiO_2 g
CSH-0.81_1d	0.81	1	50	50
CSH-0.81_3d	0.81	3	49.5	50.35
CSH-0.81_7d	0.81	7	49.5	50.35
CSH-0.81_28d	0.81	28	49.5	50.35
CSH-1.00_28d	1.00	28	55.22	44.78
CSH-1.20_28d	1.20	28	59.67	40.33
CSH-1.50_28d	1.50	28	64.90	35.10
CSH-2.40_28d	2.40	28	75.0	25.00

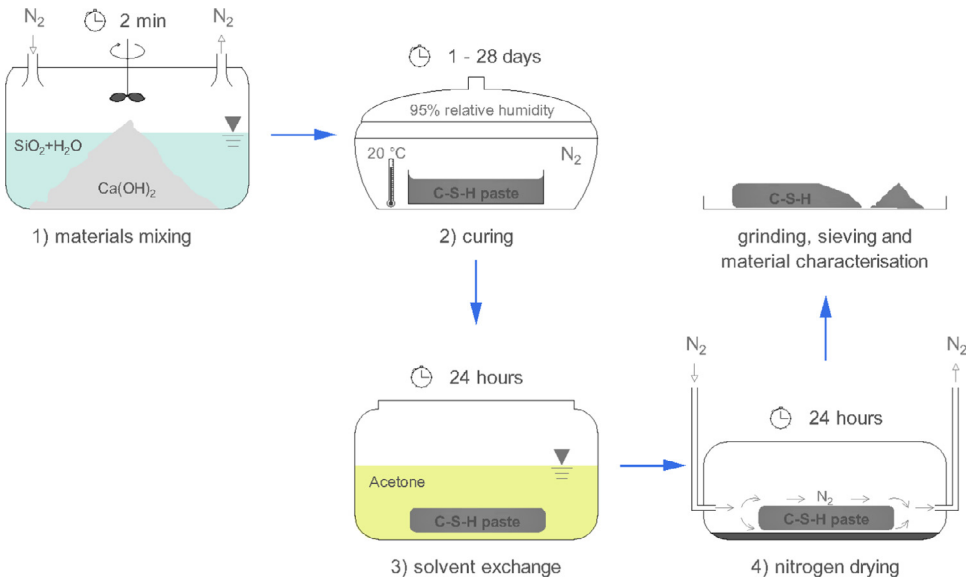

Fig. 1. Diagram explaining the synthesis process of C-S-H phases: 1) raw materials mixing; 2) sample casting and curing under controlled environmental conditions, 3) solvent exchange in acetone bath to replace pore-water and 4) nitrogen drying at room temperature.

plotted as mass loss (%) and heat flow (mW mg^{-1}) as a function of the temperature (°C). TGA/DSC measurement results were used to estimate the actual C/S molar ratio of the samples.

2.4. Powder X-ray diffraction

Powder XRD analyses were performed using a Bruker D8 Advance diffractometer with CuKα radiation over the range 5–60° 2θ, step size of 0.02° 2θ and 0.5 s $step^{-1}$. DiffracEva software from Bruker was used for XRD pattern evaluation and phase identification. Further powder XRD analysis was carried out at the UK synchrotron *Diamond Light Source*, using a 2D monochromatic high-energy beam (79.949 keV and λ = 0.15508 Å) on beamline I12, Joint Engineering, Environmental and Processing (JEEP). The detector geometry was calibrated using a diffraction pattern of CeO_2 NIST SRM 674b and the program *DAWN* was used to process collected data [19] to obtain intensity curves *I*(*Q*) [22]. For comparison reasons, intensity curves *I(Q)* were then converted into the 2θ space corresponding to a laboratory Cu anode source (λ_{Cu} = 1.5406 Å). The powdered sample was placed into a borosilicate capillary tube (ø 1.13 mm, and 80 mm in length) and sealed. Diffraction patterns were collected on samples with the lowest and the highest C/S target molar ratios of 0.81 and 2.40 respectively and compared with C-S-H synthesized by reacting calcium oxide with nano-silica suspension to achieve a target C/S = 1.07. Samples were mixed according to the synthesis process described above but calcium oxide powder was used instead of calcium hydroxide. Diffraction data were analysed using *MATLAB*. In addition, fresh samples with a target C/S = 0.81 which had been cured for 1, 3 and 28 days were also measured at beamline I12 during a different beamtime session. Samples were made in the same way (calcium hydroxide and nanosilica) and loaded into the same capillary tubes but the energy and wavelength used was 51.704 keV and 0.2266 Å respectively. Room temperature pair distribution function (PDF) data were collected during the commissioning of the XPDF beamline (I15-1) at *Diamond Light Source*. Powder samples were sealed inside borosilicate capillaries (ø0.5 mm, and 80 mm in length). X-ray scattering data were collected for C-S-H samples at C/S ratio of 0.81 and 1.0 at an energy of 66.6 keV in Rapid-Acquisition PDF geometry using a Perkin Elmer XRD1611CP3 area detector [23]. CeO_2 (NIST SRM 674b) XRD pattern was used as a calibration standard. The scattering data ($0.5 \leqslant Q \leqslant 20$ $Å^{-1}$) were corrected and processed into PDF data using the program *DAWN* [22].

2.5. Solid state NMR spectroscopy

^{29}Si MAS NMR spectra were acquired on a JEOL-600 JNM-ECZ spectrometer using a CP/MAS probe for 8 mm o.d. PSZ rotors, ν_R = 6.0 kHz and a relaxation delay of 30 s, available at Tsinghua University, Beijing, China. Chemical shifts are reported in parts per million (ppm) relative to an external sample of tetramethylsilane (TMS) using an external sample of β-Ca_2SiO_4 (δ_{iso} = −71.33 ppm) as secondary reference. The external sample of β-Ca_2SiO_4 was provided by the Institute of Mineral Resources, Beijing–China. The deconvolutions of the ^{29}Si MAS NMR spectra were performed by Lorentzian function fitting using the JEOL DELTA software.

2.6. Scanning electron microscopy

Microstructure was characterised using a scanning electron microscope (FEG-SEM, Hitachi SU6600) with energy dispersive spectroscopy (EDS, Oxford INCA-7260) and an accelerating voltage of 15–20 keV. SEM samples were prepared as follows: fresh C-S-H paste was cast into a plastic mould (ø 15 mm, thickness 2 mm) and templated onto a thin layer (*ca.* 0.125 mm) of muscovite mica at the bottom of the mould to produce a flat surface for analysis. After curing for 28 days, the specimen was dried under constant nitrogen flow, followed by vacuum drying and surface coating for SEM imaging purposes. This method has the distinct advantage of avoiding resin impregnation and polishing or drying at elevated temperatures, which can alter the micro-structure of the sample, and the muscovite mica sheet, which is atomically flat, can be easily removed from the C-S-H sample prior to analysis.

3. Results

3.1. Thermo-gravimetric measurements

Results of TG measurements are given in Fig. 2a,b and Tables 3 and 4. Thermogravimetric curves are typical of C-S-H with a total weight loss of 17–20%. The first thermal step is observed in the range 25–200 °C and corresponds to the evaporation of pore and capillary water and dehydration of C-S-H [16,24]. The second weight loss occurs between 350–550 °C and is associated with the dehydroxylation of portlandite. The thermal step in the range 600–700 °C is attributed to the loss of CO_2 from calcium carbonate, due to the surface carbonation of samples during instrument operations [16]. The weight loss values for portlandite and calcite were

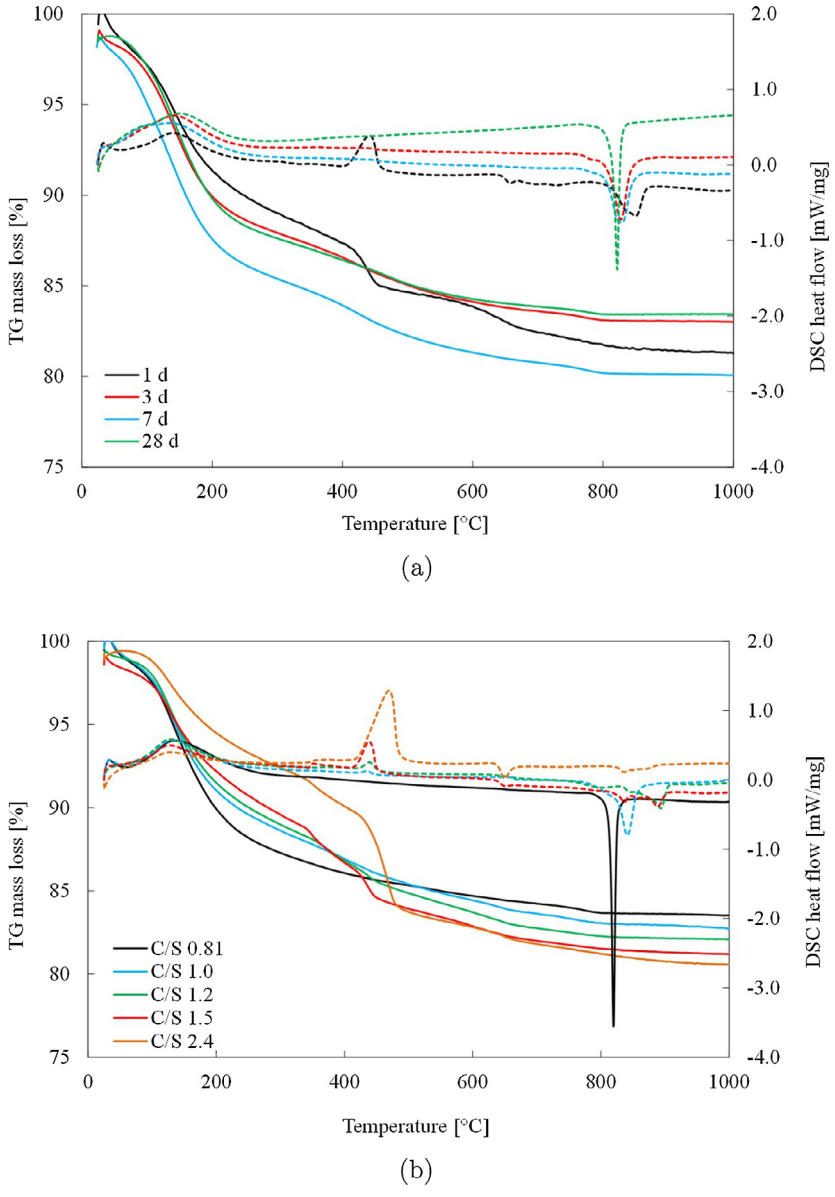

Fig. 2. Thermal curves of (a) sample at target C/S = 0.81 at different ages, and (b) samples cured for 28 days at different target C/S ratios. [TG curves: solid lines. DSC curves: dashed lines].

Table 3
Thermo-gravimetric results for each sample at different target C/S molar ratio.

Fraction of total	Target C/S ratio				
CaO as	C/S 0.81	C/S 1.0	C/S 1.2	C/S 1.5	C/S 2.4
Portlandite	0	0.151	0.203	0.215	0.397
Calcite	0	0.005	0.008	0.008	0.006
C-S-H	1	0.845	0.789	0.777	0.597
Final $\overline{C/S}$ ratio	0.81	0.87	0.98	1.22	1.60
Initial sample mass (mg)	14.40	15.80	21.90	14.20	22.40
Final sample mass (mg)	12.11	13.14	18.18	11.73	18.21

Table 4
Thermo-gravimetric results for sample C/S = 0.81 at different curing time.

Fraction of total	Curing time [days]			
CaO as	1	3	7	28
Portlandite	0.21	0.08	0.06	0
Calcite	0.05	0	0	0
C-S-H	0.74	0.92	0.94	1.00
Final $\overline{C/S}$ ratio	0.62	0.75	0.77	0.81
Initial sample mass (mg)	14.90	15.40	24.2	14.40
Final sample mass (mg)	12.20	13.02	19.33	12.11

found by a simple 3 part tangent method [25]. The weight loss was obtained as difference in weight at the intersections of the tangent drawn at the point of maximum slope in the weight loss curve and straight lines fitted to the data above and below the decomposition temperature. TGA/DSC curves for the synthetic C-S-H cured for 1, 3, 7 and 28 days are shown in Fig. 2a and TGA/DSC curves for the synthetic C-S-H with C/S mix molar ratio of 0.81, 1.0, 1.2, 1.5 and 2.4 are presented in Fig. 2b. Increasing the C/S ratio increases the total mass loss, in accordance with Garbev et al. [16]. DSC curves show two major endothermic peaks (respectively at 150–200 °C and 400–500 °C) and a major exothermic peak at 800–850 °C, which is associated with β-wollastonite formation and has been shown to form at higher temperatures with increasing C/S ratio [18]. The first broad endothermic peak is produced by the dehydration of C-S-H gel [26,16]. The area of this peak increases with ageing and decreases with increasing C/S target ratio. At the higher C/S ratios, portlandite is present and the C-S-H content is decreased as a fraction of the total sample. The second endothermic event is associated with the decomposition of portlandite [27]. By increasing the C/S ratio of the sample, the endothermic peak at 400–500 °C, becomes sharper and more well defined indicating a greater quantity of portlandite is observed, as shown in Fig. 2b. The actual C/S ratio of the C-S-H produced for each sample was calculated using a mass balance method similar to Garbev et al.[16]. It should be noted that the mass balance method assumes all nano-silica particles have reacted to form C-S-H with no remaining amorphous silica. The calculated (measured) $\overline{C/S}$ ratio for each sample is shown in Table 5 along with the target C/S ratio. Samples with a target C/S = 0.81 cured for 1 day show a well-defined step over the portlandite range and have an estimated $\overline{C/S}$ = 0.62. This value increases with curing time to a final value of 0.81. Calculated $\overline{C/S}$ ratio for samples with target C/S > 1.2 are not pure C-S-H but mixture of C-S-H + crystalline portlandite, as shown by the following X-ray diffractograms. Target C/S ratio values compared to measured $\overline{C/S}$ ratio are plotted in Fig. 3. A linear relationship is observed and the best fit regression line for the data is given by (Eq. (1)):

$$\overline{C/S} = 0.5132 \cdot C/S + 0.3868 \quad (1)$$

C-S-H with high C/S ratio (⩾1.3) is most commonly found in hydrated Portland cement rather than synthetic C-S-H, until recent research [11] has produced pure, single phase C-S-H with C/S ratio of up to 2 by inducing a high supersaturation and controlled pH during C-S-H formation. Here, high initial C/S = 2.4 leads to formation of C-S-H (at $\overline{C/S}$ = 1.60) intermixed with crystalline portlandite. It is acknowledged that determining the C/S ratio of the sample using more than one technique, such as carrying out TEM analyses, would improve the accuracy of the C/S ratio determination.

Table 5
Summary of the target and calculated C/S molar ratios from thermo-gravimetric analysis.

Sample	Target C/S ratio	Calculated $\overline{C/S}$ ratio
CSH-0.81_28d	0.81	0.81
CSH-1.00_28d	1.00	0.87
CSH-1.20_28d	1.20	0.98
CSH-1.50_28d	1.50	1.22
CSH-2.40_28d	2.40	1.60

3.2. XRD characterisation of synthetic C-S-H

Laboratory XRD measurements were taken from samples at target C/S ratio = 0.81 at different curing time (1, 3, 7 and 28 days) are shown in Fig. 4a, while the effect of increasing C/S ratio on the crystalline structure is reported in Fig. 4b, for samples at different target C/S ratios. High energy synchrotron XRD patterns of C-S-H at C/S mix ratios of 0.81 and 2.40 are shown in Fig. 5a and are com-

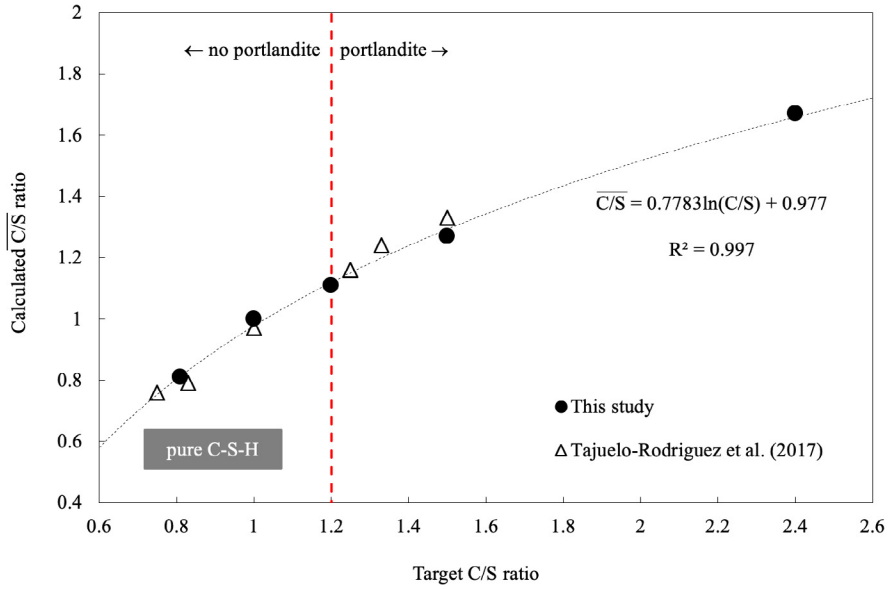

Fig. 3. Calculated $\overline{C/S}$ molar ratio values plotted as a function of the target C/S ratio of the C-S-H in samples aged 28 days.

pared to C-S-H obtained by mixing calcium oxide and nano-silica using a C/S = 1.07, following the synthesis process previously described. Reflection *d*-spacing values were determined by using linear interpolation on both sides of the peak to remove the background and fitting the peak to a Voigt distribution. In the synchrotron XRD patterns, C-S-H reflections are observed at *ca.* 7, 16, 29, 32, 49, 54, 60, 66° 2θ and a 'hump' is also visible at *ca.* 43° 2θ. The lowest angle peak is the basal spacing of C-S-H which describes the inter-layer spacing and the strongest peak at *ca.* 29° 2θ is regarded as (110) [18], *d*-spacing values for both are reported in Table 6 from synchrotron data. The basal spacing decreases from 14.0 Å to 12.8 Å with increasing C/S ratio. This shrinking behaviour can arise from removal of silicate bridging tetrahedra in the C-S-H structure, plus inclusion of Ca in the inter-layer spacing or inter-stratification of layers of tobermorite dimers and tobermorite infinite layers [18]. The basal reflection *d*-spacing and C/S ratio of the lower C/S sample (C/S = 0.81 and 1.07, and which contained no portlandite in the XRD patterns) fall between the upper dashed trendline and middle solid trendline of Fig. 2 in [18] which plots C/S ratio against *d*-spacing. The C/S ratio for the sample C/S = 1.07 is not measured with TGA but as the measured $\overline{C/S}$ value of the C/S = 1.0 sample is 0.87, the actual $\overline{C/S}$ ratio of this sample cannot differ significantly. The highest mix C/S ratio sample (=2.4) has a (TGA) measured $\overline{C/S}$ = 1.60 and a basal spacing of 12.8 Å, which is larger than the *ca.* 11.5–12.0 expected from analysis of several authors datasets, presented in [18,28]. However, the amount of Ca in the starting mix is particularly high, and it is therefore probable the sample was an intermixture of C-S-H and portlandite, as described by [28].

We also observe a decrease in *d*-spacing of the main reflection at *ca.* 29° 2θ which is attributed to shrinkage in the crystallographic *b*-direction (*ca.* 1.0%), also from omission of bridging

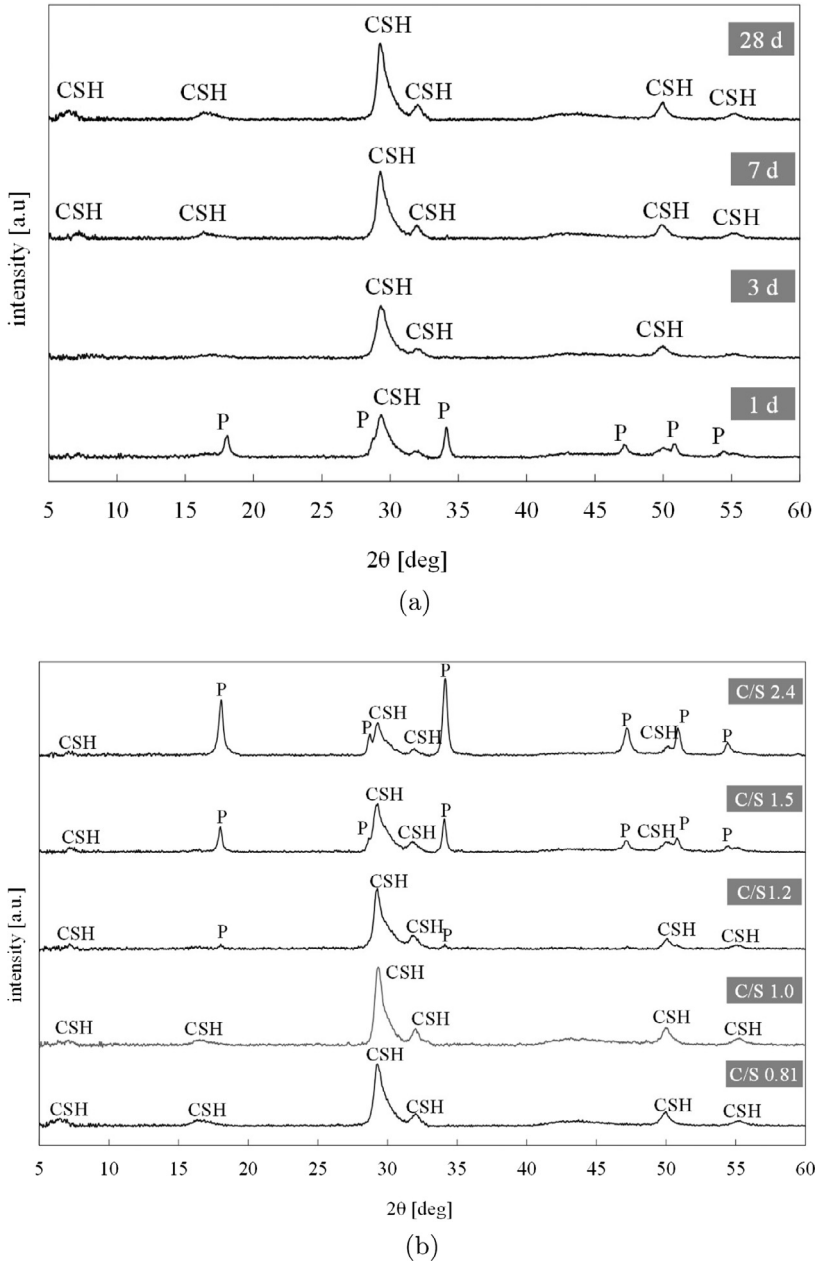

Fig. 4. Laboratory XRD patterns of (a) sample at target C/S = 0.81 at different ages, in days, and (b) samples cured for 28 days at different target C/S ratios. [P: portlandite reflection; CSH: calcium silicate hydrate reflection].

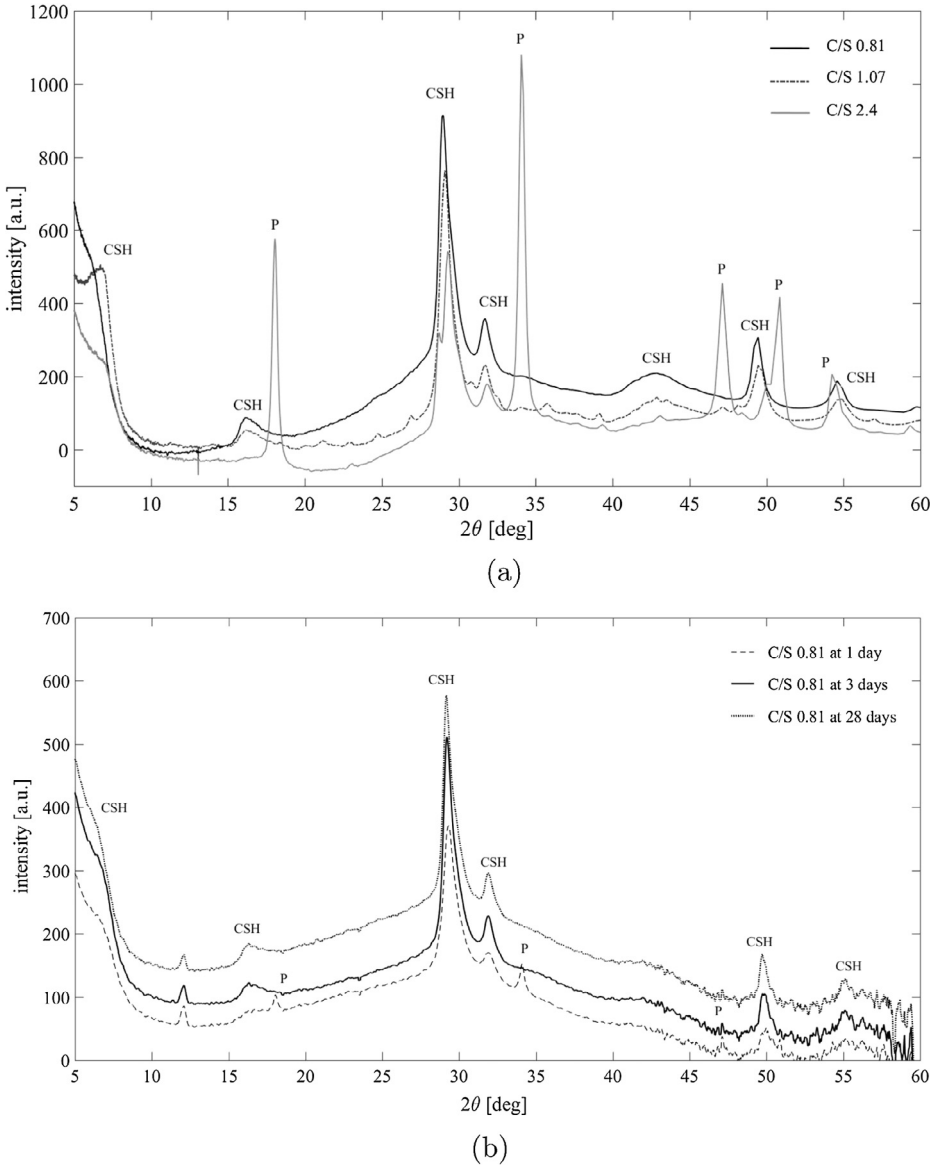

Fig. 5. Synchrotron XRD measurements of (a) samples at C/S target ratios of 0.81, 1.07 and 2.40 cured for 28 days, and (b) samples at target C/S = 0.81 cured for 1, 3 and 28 days. [P: portlandite reflection; CSH: calcium silicate reflection].

Table 6
Synchrotron X-ray diffraction patterns acquired at Diamond Light Source (Oxfordshire, UK) using beamline I12. Basal spacing is reported in d-spacing (Å) along with the main reflection at *ca.* 29° 2θ. The synchrotron XRD data was collected at two different beamtime sessions on fresh samples poured and cured for each session. The first 3 rows (target C/S = 0.81 to 2.4, all cured for 28 days) were collected separately to the curing time study given in the last 3 rows for samples with target C/S = 0.81 and cured for 1, 3, 28 days. The basal spacing is relatively weak and has some asymmetry.

Synchrotron XRD	Basal reflection, *d*-spacing Å	Main reflection, *d*-spacing Å
C/S 0.81 (28 days)	13.96	3.08
C/S 1.07 (28 days)	13.05	3.07
C/S 2.4 (28 days)	12.83	3.05
C/S 0.81 (1 day)	12.94	3.05
C/S 0.81 (3 days)	13.18	3.06
C/S 0.81 (28 days)	13.69	3.06

tetrahedra. In accordance with Garbev et al. and Soyer-Uzun et al. this shift to lower *d*-spacing is correlated with increasing C/S ratio [15,29]. We observe flattening of the hump at *ca.* 44° 2θ and the broad reflection at *ca.* 16° 2θ with increasing C/S ratio. Flattening of the hump is ascribed to a reduction in amorphous material [18] while reduced intensity reflections at *ca.* 16° 2θ are associated with decreasing Si occupancy in the bridging sites [13], resulting in a depolymerisation effect. There is a clear reduction in intensity of the peak at 16° 2θ in Fig. 5a between samples C/S = 0.81 and 1.07, but the C/S = 2.4 sample has almost no peak visible at 16° 2θ. The relative intensity of the reflection at *ca.* 16° 2θ for the sample with C/S = 1.07, as described by [13]:

$$I_{rel} = \left[\left(I_{16.1^\circ_i}/I_{29.2^\circ_i}\right)_{Ca/Si_i}\right] / \left[\left(I_{16.1^\circ_{0.81}}/I_{29.2^\circ_{0.81}}\right)_{Ca/Si_{0.81}}\right] \quad (2)$$

is 0.5 for the synchrotron XRD patterns (samples C/S = 1.07/0.81) and 0.7 for the laboratory XRD patterns (samples C/S = 1.0/0.81) which fits quite well with the trendline shown by Grangeon et al. [13]. The values themselves are reasonably comparable with existing literature [13] but the trend is more obvious: that the reflection at *ca.* 16° 2θ reduces with increasing C/S ratio compared to the main reflection at *ca.* 29° 2θ suggesting de-polymerisation with increasing C/S ratio [13].

Two replica curing time studies were conducted, using the same starting C/S composition (target C/S = 0.81) and analysed after curing for 1, 3 and 28 days (synchrotron XRD) and after curing for 1, 3, 7 and 28 days (laboratory XRD). In all cases, hydration was arrested with acetone and samples were dried at room temperature under a nitrogen gas stream, as previously described. Results are shown in Fig. 5b. Both curing time studies show portlandite is present after 1 day of curing, but is not present (XRD) from day 3 onwards. The basal spacing increases with increased curing time from 12.9 Å (1 day) to 13.2 Å (3 days) and to 13.7 Å (28 days) from the synchrotron XRD patterns and d-spacing of the reflection at ca. 29° 2θ increases slightly with sample age which perhaps shows the polymerisation process with sample ageing.

Sample composition was estimated from XRD data from peak areas as described in Maddalena et al. [30] by using the area of the strong peak at *ca.* 29° 2θ for each pattern compared with that from the pure phase sample (C/S 0.81 at 28 days) calibrated against the known quantity of CaO in the starting mix. The results are shown in Table 7 and 8 and compare reasonably well with the thermogravimetry results, shown in Table 3 and 4. The main differences are that calcite is not present in the XRD patterns, while minor quantities are found in the TGA and the amount of portlandite in the sample is often higher in the TGA results which can be explained if there is any amorphous portlandite [28] present in the samples that XRD will not detect.

3.3. PDF data

Integrated, normalised, pair distribution function data was fitted using both 11 Å and 14 Å tobermorite models (ICSD collection codes 92942 and 152489) with the 11 Å providing a slightly better fit (R_{wp} value) as shown in Table 9 and Figs. 6 and 7, but the difference is slight and the fit to tobermorite gets increasingly poor after 8 Å. The existence of correlations up to around 40 Å shows that medium-range order is present within these materials, although it is likely that ordering on this length-scale is only present within calcium silicate hydrates layers [31]. Modelling the pair distribution function data as a nanocrystalline material produces ordered domains of radii 25–45 Å depending on the structure file used, as shown in Table 9. This fits well with the particle diameter of 35 Å determined by Skinner et al. [32] for synthetic C-S-H (C/S = 1) using X-ray diffraction who describe it as similar to a size broadened 11 Å tobermorite crystal. For comparison with existing C-S-H models, the data was fitted to the structures described in Grangeon et al. [31] where for each data set, 4 independent fits were carried out in which the occupancy of the Si bridging and paired tetrahedra were constrained differently. In 2 of the 4 fits, only the occupancy of the bridging Si (1) or paired Si (2) was refined with the other set to 1. In the third, the occupancy of both sites was constrained to be equal and in the fourth, both occupancies were refined simultaneously. These are listed in Table 9 as Grangeon_s1 to Grangeon_s4. Richardson [28] developed 16 structural models for C-S-H, using crystal chemical reasoning from 2 end member structures based on tobermorite with either infinite silicate chains (C/S ratio = 2/3 and no interlayer calcium - denoted T∞) or an entirely dimeric structure (called T2, C/S ratio = 1.5). Of the 16 models presented, we fit our data to the intermediate structures constructed from mixes of the 2 end members and are based on either 11 Å or 14 Å tobermorite: T5-14sc, T5-11sc, T3-14sc, T11-14sc; as the C/S ratio of our samples is broadly in the range of the intermediate models. The best fit overall is 11 Å tobermorite but the monoclinic cell allowed refinement of the atomic coordinates, which naturally produces a better fit, and is not feasible for the *P*1 spacegroup assigned to the C-S-H structures. The best fit of the 8 C-S-H structures presented was Richardson's T5-14sc on the basis that it has the lowest R_{wp} value and the refined spherical domain radius is the largest, indicating that this structure also fits the sample over longer distances than the others.

Peaks located at *ca.* 1.66 Å and *ca.* 2.44 Å correspond to Si–O and Ca–O correlations, respectively [31,29]. The interatomic bond dis-

Table 9
Spherical domain radius and goodness of fit (R_{wp}) are reported for each sample depending on the crystallographic information file the data is fitted to. Estimated uncertainty of the last digit from the least square refinement is reported in brackets. The 11 Å tobermorite fit is slightly better and is regarded as the closest match for synthetic C-S-H [29].

Sample	C/S 0.81		C/S 1.0	
	R_{wp}	Size/Å	R_{wp}	Size/Å
Tobermorite 11 Å	32.77	29.6(13)	32.62	30.9(15)
Tobermorite 14 Å	33.12	23.3(6)	34.01	23.5(6)
Grangeon_s1	51.09	16.6(6)	53.03	16.4(5)
Grangeon_s2	50.49	16.1(6)	53.12	17.1(7)
Grangeon_s3	52.72	17.4(7)	53.73	16.9(7)
Grangeon_s4	53.38	16.5(7)	54.06	16.3(5)
Richardson_T3_14sc	50.94	34(3)	50.89	34(3)
Richardson_T5_11sc	48.98	39(4)	48.76	39(4)
Richardson_T5_14sc	42.39	43(3)	42.25	42(3)
Richardson_T11_14sc	47.80	28(2)	48.15	28(2)

Table 7
Laboratory XRD results for each sample at different target C/S molar ratio. Where very small quantities of portlandite are found but not clear in the XRD diffratograms, it is because pattern analysis is approximate and that the C-S-H reflection being monitored appeared to decreased in area (sample C/S = 1.0).

Fraction of total	*Target C/S ratio*				
CaO as	C/S 0.81	C/S 1.0	C/S 1.2	C/S 1.5	C/S 2.4
Portlandite	0	0.01	0.20	0.21	0.43
Calcite	0	0	0	0	0
C-S-H	1.0	0.99	0.80	0.79	0.57

Table 8
Laboratory XRD results for sample C/S = 0.81 at different curing time.

Fraction of total	*Curing time [days]*			
CaO as	1	3	7	28
Portlandite	0.19	0.06	0.02	0
Calcite	0	0	0	0
C-S-H	0.74	0.92	0.94	1.00

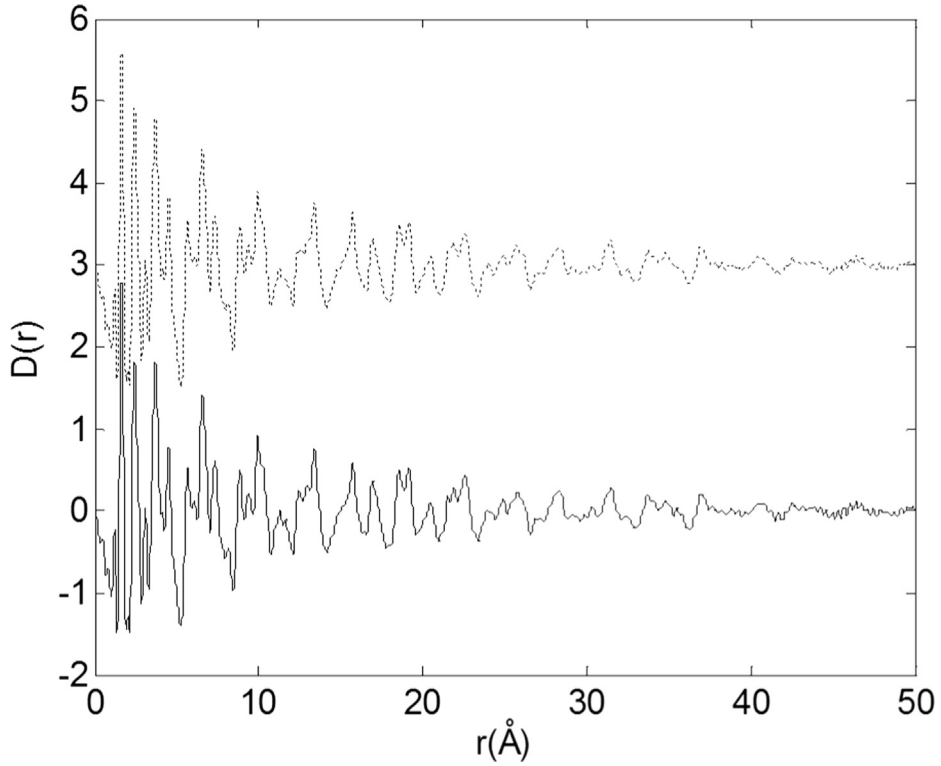

Fig. 6. The solid black line is sample C/S 0.81, dotted black line is sample C/S 1.0. Correlations extend beyond 30 Å but the fit to tobermorite 11 Å gets increasingly poor after 8 Å, further demonstrating the limited ordering of C-S-H compared to tobermorite. *D(r)* is plotted according to the formalism outlined in Keen (2001) [33] where *D(r)* is described as the differential correlation function, sometimes labelled in other publications as *G(r)*. Unlike some other formalisms of the PDF, *D(r)* is scaled according to *r* and therefore emphasizes the high *r*-region; the medium *r*-region is the most valuable region for C-S-H analysis as it contains information of ordering between layers. The *y*-axis is the same as that used by Grangeon et al. [31] which they label *g(r)*.

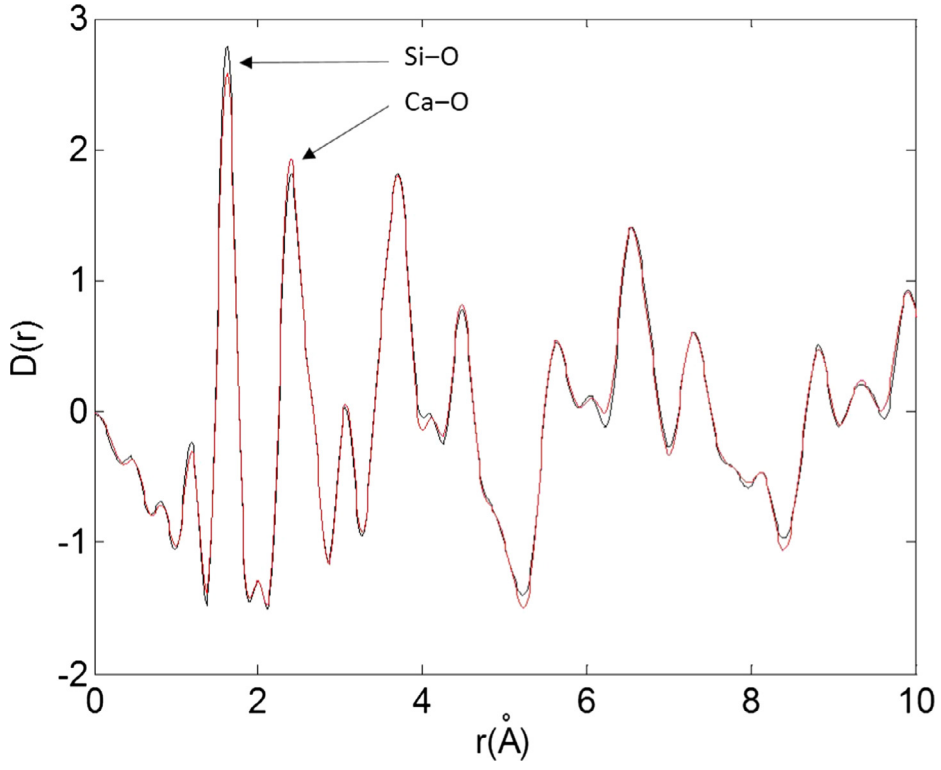

Fig. 7. Magnification of Fig. 6 of the region from 0 to 10 Å. Sample C/S 0.81 is black and sample C/S 1.0 is red. Si–O (1.6 Å) and Ca–O (2.4 Å) correlations are marked with arrows.The difference in intensity of the Ca–O and Si–O correlations between the two samples (shown with arrows) shows the relative abundance of that atom pair within the sample.

Table 10
The inter-atomic bond distances (in Å) are taken from the position of the peaks for each atom pair and determined by fitting the peaks to a Gaussian distribution which also gives the peak intensity values. Goodness of fit (R^2) is given in brackets for each peak.

Sample	Inter-atomic bond distances		Intensities	
	Ca–O	Si–O	Ca–O	Si–O
C/S 0.81	2.37(0.93)	1.62(0.98)	1.99(0.93)	4.49(0.98)
C/S 1.0	2.37 (0.94)	1.62(0.98)	2.06(0.94)	4.16(0.98)

tances obtained from the fit for Si–O and Ca–O are given in Table 10 along with the peak intensities which indicate the relative abundance of each atomic pair. As observed before [31,29] the greater intensity of Ca–O and lower intensity of Si–O in C/S = 1.0 compared with C/S = 0.81 shows the relative quantities of Ca and Si in the samples in line with their target and measured C/S values.

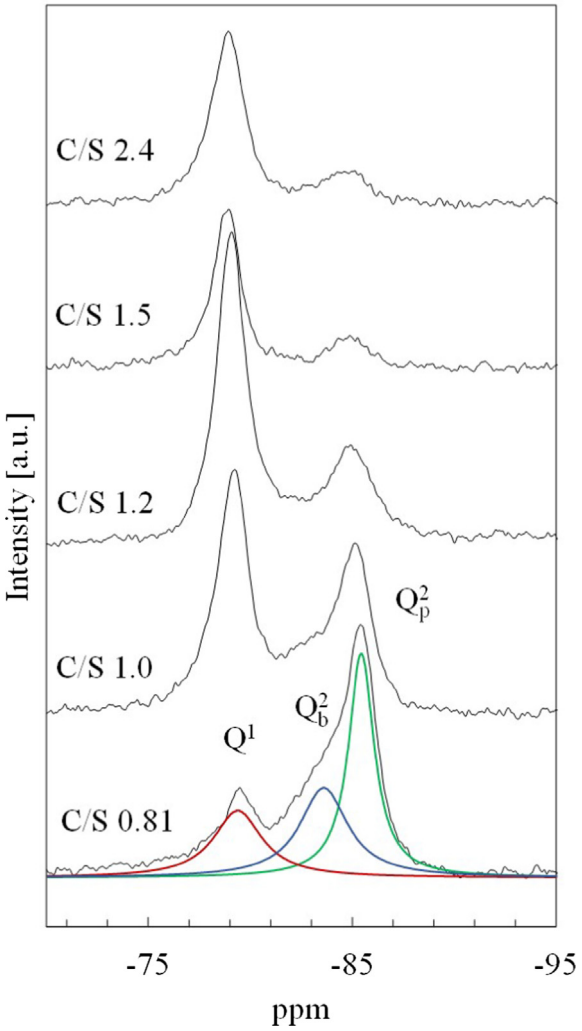

Fig. 8. ^{29}Si MAS NMR spectra (ν_R = 6.0 kHz, 30 s relaxation delay) of C-S-H samples at different target C/S molar ratios ranging from 0.81 to 2.4. The spectra are obtained for samples cured for 28 days.

3.4. NMR measurements

Results of ^{29}Si MAS NMR measurements of the samples at different target C/S molar ratio are displayed in Fig. 8. In samples with low C/S ratio (=0.81 and 1.0) three different peaks are resolved, corresponding to end groups of SiO_4 tetrahedra (Q^1 sites, δ_{iso} = −79.5 ppm), bridging and paired SiO_4 tetrahedra (respectively Q_b^2 sites and Q_p^2 sites, δ_{iso} = −82.8 ppm and δ_{iso} = −85.2 ppm) [6,34,28].Increasing C/S ratio results in more Q^1 sites and fewer Q_b^2 sites, meaning that the silicate chains become shorter and the molecular structure of C-S-H is mainly composed of silicate dimers. The synthesised C-S-H shows a defect tobermorite-like structure de-polymerises with increasing C/S ratio by omission of bridging tetrahedra beyond target C/S = 1.2, in accordance with previous studies [35,31,11]. NMR chemical shifts move to less negative values as a result of more Ca incorporation in the interlayer [36] which is observed for both Q^1 and Q^2 sites as the C/S ratio increases. Deconvolution of the NMR spectra allowed us to calculate the degree of polymerisation by calculating the mean silica chain length using Eq. 3:

$$MCL = \frac{2\left[I\left(Q^1\right) + I\left(Q_b^2\right) + I\left(Q_p^2\right)\right]}{I\left(Q^1\right)} \quad (3)$$

where *MCL* is the mean chain length of SiO_4 tetrahedra and *I* is the relative intensity of the Q^1, Q_b^2 and Q_p^2 resonances of the C-S-H. In Table 11 the mean chain length *MCL* is reported for each C/S target ratio and values are in agreement with other reported results [35,36,28] where *MCL* decreases to *ca.* 2–3 at *ca.* C/S = 1.2 and after which no further de-polymerisation takes place with increasing C/S ratio. The fraction of vacant tetrahedral sites (v) is calculated using the Eq. 3

$$v = \frac{1}{MCL + 1} \quad (4)$$

as reported in Richardson, 2014 [28].

3.5. SEM analysis

The pore structure of synthetic C-S-H is different from C-S-H phases found in hydrated Portland cement. Scanning electron microscopy images show a very porous structure, which reflects the low density of the synthesised material (Fig. 9a). EDX analysis confirmed the presence of C-S-H phases. Plate-like C-S-H structures were observed in all the samples after 28 days of curing (Fig. 9b), similar to those described in Grangeon et al., 2013 [37]. Open porosity value was measured for sample with C/S = 0.81 as 0.74 (as reported in Maddalena et al., 2018, sample CHNS, [38]).

Table 11
Mean silicate chain length (MCL) of C-S-H samples at different target C/S molar ratios and relative intensities (I) of Q^1, Q_b^2 and Q_p^2 sites, and fraction of vacant tetrahedral sites (v).

Sample	$I(Q^1)$ %	$I(Q_b^2)$ %	$I(Q_p^2)$ %	MCL –	v –
C/S 0.81	17.43	21.93	60.64	11.5	0.08
C/S 1.0	53.73	9.89	36.38	3.7	0.21
C/S 1.2	75.44	2.88	21.68	2.7	0.27
C/S 1.5	84.43	1.00	15.57	2.4	0.29
C/S 2.4	83.71	1.00	16.29	2.4	0.29

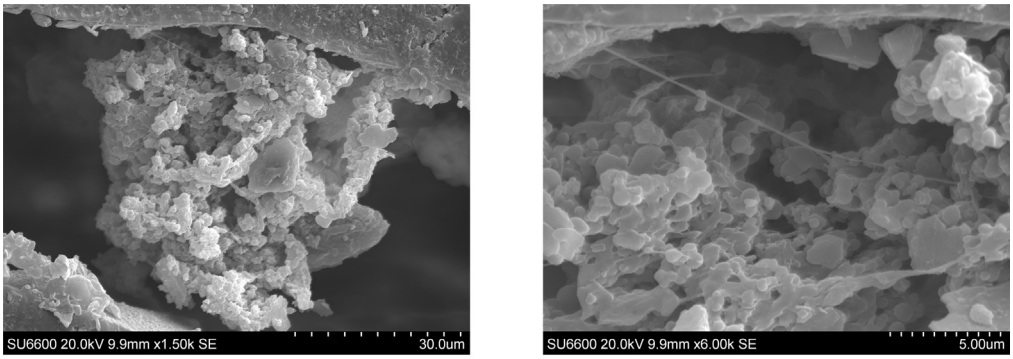

Fig. 9. SEM image of (a) sample CSH-0.81_28 and (b) magnification of SEM image of sample CSH-0.81_28. C-S-H phase with plate-like structure.

4. Conclusions

Synthesis of pure, solid C-S-H has been presented and the product has been characterised. C-S-H was prepared by mixing a dry source of calcium and aqueous nano-silica suspension with deionised and decarbonated water, manually and without further chemical processing, providing a simple, relatively fast and inexpensive method for producing solid C-S-H. A combined nitrogen-solvent exchange drying method was used to dry the samples, preserving the pore structure and preventing surface carbonation. While similar starting ingredients have certainly been used before [13,6,14–18] the C-S-H is produced by using a very high water to solid ratio of *ca.* w/s = 3–8 + which produces a slurry that has to be filtered or is mechanically milled then filtered [14–16]. In addition, no other work explores solid samples made with an abundance of Ca (sample C/S = 2.4) plus ageing from 1 day curing time. From TGA and XRD analysis, C-S-H at low C/S ratio is formed after 1 day curing and after 3 days no portlandite is detected by XRD (laboratory or synchrotron). Polymerisation with increased curing time is suggested by the synchrotron XRD results. Depolymerisation with increasing C/S ratio (samples cured for 28 days) by omission of bridging SiO_4 tetrahedra is supported by XRD and ^{29}Si MAS NMR data, which is consistent with the literature. Spherical domain radius is estimated from X-ray PDF to be 2.5–4.5 nm and the medium range nature of structural order is also indicated, which is consistent with previous PDF analyses. The synthesis process has the advantage of being relatively fast (7 days curing + 1 day drying), easy to develop without further equipment or complex procedures, and short manufacturing time. Importantly, it could also be upscaled to industrial batch mixing and the product has various applications, including the construction industry and waste-water purification technologies.

Acknowledgment

This work is supported by UK-EPSRC (Grant No. EP/L014041/1-DISTINCTIVE Consortium). Data associated with research published and supporting information in this paper are accessible at https://doi.org/10.15129/e85d5f91-5dfd-46cc-bc7e-46ed3a92e5d8. The authors wish to acknowledge the support of the European Commission via the Marie Curie IRSES project GREAT-*Geotechnical and geological Responses to climate change: Exchanging Approaches and Technologies on a world-wide scale* (FP7-PEOPLE-2013-IRSES-612665). The support of Research Fund of Tsinghua University, Grant No. 2014Z01004 is acknowledged. The authors thank Diamond Light Source for access to beamline I12 (proposal ee12533-4) and I15-1 (rapid access) that contributed to the results presented here. Further acknowledgment to the support of the Diamond Light Source personnel, Dr. Oxana Magdysyuk, with data processing and analysis.

References

[1] Z. Zhang, J.L. Provis, A. Reid, H. Wang, Geopolymer foam concrete: an emerging material for sustainable construction, Constr. Build. Mater. 56 (2014) 113–127, https://doi.org/10.1016/j.conbuildmat.2014.01.081.
[2] J.J. Chen, J.J. Thomas, H.F. Taylor, H.M. Jennings, Solubility and structure of calcium silicate hydrate, Cem. Concr. Res. 34 (9) (2004) 1499–1519, https://doi.org/10.1016/j.cemconres.2004.04.034.
[3] A. Stumm, K. Garbev, G. Beuchle, L. Black, P. Stemmermann, R. Nüesch, Incorporation of zinc into calcium silicate hydrates, Part I: formation of C-S-H (I) with C/S=2/3 and its isochemical counterpart gyrolite, Cem. Concr. Res. 35 (9) (2005) 1665–1675, https://doi.org/10.1016/j.cemconres.2004.11.007.
[4] E. Wieland, J. Tits, D. Kunz, R. Dähn, Strontium uptake by cementitious materials, Environ. Sci. Technol. 42 (2) (2008) 403–409, https://doi.org/10.1021/es071227y.
[5] Y. Zhou, D. Hou, J. Jiang, P. Wang, Chloride ions transport and adsorption in the nano-pores of silicate calcium hydrate: experimental and molecular dynamics studies, Constr. Build. Mater. 126 (2016) 991–1001, https://doi.org/10.1016/j.conbuildmat.2016.09.110.
[6] X. Cong, R. Kirkpatrick, 29Si MAS NMR study of the structure of calcium silicate hydrate, Adv. Cem. Based Mater. 3 (3–4) (1996) 144–156, https://doi.org/10.1016/S1065-7355(96)90046-2.
[7] A. Harris, M. Manning, W. Tearle, C. Tweed, Testing of models of the dissolution of cements-leaching of synthetic CSH gels, Cem. Concr. Res. 32 (5) (2002) 731–746, https://doi.org/10.1016/S0008-8846(01)00748-7.
[8] L. Nicoleau, G. Albrecht, K. Lorenz, D. Fridrich, T. Wohlhaupter, R. Dorfner, H. Leitner, M. Vierle, D. Schmitt, M. Braeu, C. Hesse, S. Montero, S. Zuern, M. Kutschera, US Patent 2011/0269875 A1 – Plasticizer-containing hardening accelerator composition, 2014..
[9] V. Kanchanason, J. Plank, Role of pH on the structure, composition and morphology of C-S-H PCE nanocomposites and their effect on early strength development of Portland cement, Cem. Concr. Res. 102 (February) (2017) 90–98, https://doi.org/10.1016/j.cemconres.2017.09.002.
[10] S. Tränkle, D. Jahn, T. Neumann, L. Nicoleau, N. Hüsing, D. Volkmer, Conventional and microwave assisted hydrothermal syntheses of 11 Å tobermorite, J. Mater. Chem. A 1 (35) (2013) 10318, https://doi.org/10.1039/c3ta11036b.
[11] A. Kumar, B.J. Walder, A. Kunhi Mohamed, A. Hofstetter, B. Srinivasan, A.J. Rossini, K. Scrivener, L. Emsley, P. Bowen, The atomic-level structure of cementitious calcium silicate hydrate, J. Phys. Chem. C 121 (32) (2017) 17188–17196, https://doi.org/10.1021/acs.jpcc.7b02439.
[12] W. Kunther, S. Ferreiro, J. Skibsted, Influence of the Ca/Si ratio on the compressive strength of cementitious calcium-silicate-hydrate binders, J. Mater. Chem. A 5 (2017) 17401–17412, https://doi.org/10.1039/C7TA06104H.
[13] S. Grangeon, F. Claret, C. Roosz, T. Sato, S. Gaboreau, Y. Linard, Structure of nanocrystalline calcium silicate hydrates: insights from X-ray diffraction, synchrotron X-ray absorption and nuclear magnetic resonance, J. Appl. Crystallogr. 49 (2016) 771–783, https://doi.org/10.1107/S1600576716003885.
[14] K. Garbev, P. Stemmermann, L. Black, C. Breen, J. Yarwood, B. Gasharova, Structural features of C-S-H(I) and its carbonation in air-A Raman spectroscopic study. Part I: Fresh phases, J. Am. Ceram. Soc. 90 (3) (2007) 900–907, https://doi.org/10.1111/j.1551-2916.2006.01428.x.
[15] K. Garbev, M. Bornefeld, G. Beuchle, P. Stemmermann, Cell dimensions and composition of nanocrystalline calcium silicate hydrate solid solutions. Part 1: Synchotron-based X-Ray diffraction, J. Am. Ceram. Soc. 91 (9) (2008) 3005–3014, https://doi.org/10.1111/j.1551-2916.2008.02601.x.

[16] K. Garbev, M. Bornefeld, G. Beuchle, P. Stemmermann, Cell dimensions and composition of nanocrystalline calcium silicate hydrate solid solutions. Part 2: X-ray and thermogravimetry study, J. Am. Ceram. Soc. 91 (9) (2008) 3015–3023, https://doi.org/10.1111/j.1551-2916.2008.02601.x.
[17] E. Tajuelo Rodriguez, I.G. Richardson, L. Black, E. Boehm-Courjault, A. Nonat, J. Skibsted, Composition, silicate anion structure and morphology of calcium silicate hydrates (C-S-H) synthesised by silica-lime reaction and by controlled hydration of tricalcium silicate (C3S), Adv. Appl. Ceram. 114 (7) (2015) 362–371, https://doi.org/10.1179/1743676115Y.0000000038.
[18] E. Tajuelo, K. Garbev, D. Merz, L. Black, I.G. Richardson, Thermal stability of C-S-H phases and applicability of Richardson and Groves' and Richardson C-(A)-S-H (I) models to synthetic C-S-H, Cem. Concr. Res. 93 (2017) 45–56, https://doi.org/10.1016/j.cemconres.2016.12.005.
[19] X. Pardal, I. Pochard, A. Nonat, Experimental study of Si-Al substitution in calcium-silicate-hydrate (C-S-H) prepared under equilibrium conditions, Cem. Concr. Res. 39 (8) (2009) 637–643, https://doi.org/10.1016/j.cemconres.2009.05.001.
[20] O. Mendoza, C. Giraldo, S.S. Camargo, J.I. Tobón, Structural and nano-mechanical properties of Calcium Silicate Hydrate (C-S-H) formed from alite hydration in the presence of sodium and potassium hydroxide, Cem. Concr. Res. 74 (2015) 88–94, https://doi.org/10.1016/j.cemconres.2015.04.006.
[21] S. Nath, S. Maitra, S. Mukherjee, S. Kumar, Microstructural and morphological evolution of fly ash based geopolymers, Constr. Build. Mater. 111 (2016) 758–765, https://doi.org/10.1016/j.conbuildmat.2016.02.106.
[22] J. Filik, A. Ashton, P. Chang, P. Chater, S. Day, M. Drakopoulos, M. Gerring, M. Hart, O. Magdysyuk, S. Michalik, Processing two-dimensional X-ray diffraction and small-angle scattering data in DAWN 2, J. Appl. Crystallogr. 2 (50) (2017) 959–966, https://doi.org/10.1107/S1600576717004708.
[23] P.J. Chupas, X. Qiu, J.C. Hanson, P.L. Lee, C.P. Grey, S.J.L. Billinge, Rapid-acquisition pair distribution function (RA-PDF) analysis, J. Appl. Crystallogr. (36(6), 2003,) 1342–1347, https://doi.org/10.1107/S0021889803017564. arXiv:0304638v1.
[24] H. Biricik, N. Sarier, Comparative study of the characteristics of nano silica, silica fume, and fly ash incorporated cement mortars, Mater. Res. 17 (3) (2014) 570–582, https://doi.org/10.1590/S1516-14392014005000054.
[25] B. Lothenbach, P. Durdzinski, K. de Weerdt, Thermogravimetric analysis, in: A practical Guide to Microstructural Analysis of Cementitious Materials, CRC Press – Taylor & Francis group, 2015, pp. 177–211. Ch. 5.
[26] S. Ma, W. Li, S. Zhang, Y. Hu, X. Shen, Study on the hydration and microstructure of Portland cement containing diethanol-isopropanolamine, Cem. Concr. Res. 67 (2015) 122–130, https://doi.org/10.1016/j.cemconres.2014.09.002.
[27] F. Saito, G. Mi, M. Hanada, Mechanochemical synthesis of hydrated calcium silicates by room temperature grinding, Solid State Ionics 101 (1997) 37–43, https://doi.org/10.1016/S0167-2738(97)84006-4.
[28] I.G. Richardson, Model structures for C-(A)-S-H(I), Acta Crystallographica Section B: structural science, Crystal Eng. Mater. 70 (6) (2014) 903–923, https://doi.org/10.1107/S2052520614021982.
[29] S. Soyer-Uzun, S.R. Chae, C.J. Benmore, H.R. Wenk, P.J.M. Monteiro, Compositional evolution of calcium silicate hydrate (C-S-H) structures by total X-ray scattering, J. Am. Ceram. Soc. 95 (2) (2012) 793–798, https://doi.org/10.1111/j.1551-2916.2011.04989.x.
[30] R. Maddalena, C. Hall, A. Hamilton, Effect of silica particle size on the formation of calcium silicate hydrate (C-S-H) using thermal analysis, Thermochim. Acta 672 (2019) (2018) 142–149, https://doi.org/10.1016/j.tca.2018.09.003.
[31] S. Grangeon, A. Fernandez-Martinez, A. Baronnet, N. Marty, A. Poulain, E. Elkaim, C. Roosz, S. Gaboreau, P. Henocq, F. Claret, Quantitative X-ray pair distribution function analysis of nanocrystalline calcium silicate hydrates: a contribution to the understanding of cement chemistry, J. Appl. Crystallogr. 50 (22) (2017) 14–21, https://doi.org/10.1107/S1600576716017404.
[32] L.B. Skinner, S.R. Chae, C.J. Benmore, H.R. Wenk, P.J.M. Monteiro, Nanostructure of calcium silicate hydrates in cements, Phys. Rev. Lett. 104 (19) (2010), https://doi.org/10.1103/PhysRevLett. 104.195502. URL: http://link.aps.org/doi/10.1103/PhysRevLett.104.195502 195502.
[33] D.A. Keen, A comparison of various commonly used correlation functions for describing total scattering, J. Appl. Crystallogr. 34 (2) (2001) 172–177, https://doi.org/10.1107/S0021889800019993.
[34] I. Richardson, L. Black, J. Skibsted, R. Kirkpatrick, Characterisation of cement hydrate phases by TEM, NMR and Raman spectroscopy, Adv. Cem. Res. 22 (4) (2010) 233–248, https://doi.org/10.1680/adcr.2010.22.4.233.
[35] T.F. Sevelsted, J. Skibsted, Carbonation of C-S-H and C-A-S-H samples studied by 13C, 27Al and 29Si MAS NMR spectroscopy, Cem. Concr. Res. 71 (2015) 56–65, https://doi.org/10.1016/j.cemconres.2015.01.019.
[36] E. L'Hôpital, B. Lothenbach, D. Kulik, K. Scrivener, Influence of calcium to silica ratio on aluminium uptake in calcium silicate hydrate, Cem. Concr. Res. 85 (2016) 111–121, https://doi.org/10.1016/j.cemconres.2016.01.014.
[37] S. Grangeon, F. Claret, C. Lerouge, F. Warmont, T. Sato, S. Anraku, C. Numako, Y. Linard, B. Lanson, On the nature of structural disorder in calcium silicate hydrates with a calcium/silicon ratio similar to tobermorite, Cem. Concr. Res. 52 (2013) 31–37, https://doi.org/10.1016/j.cemconres.2013.05.007.
[38] R. Maddalena, J.J. Roberts, A. Hamilton, Can Portland cement be replaced by low-carbon alternative materials? A study on thermal properties and carbon emissions of innovative cements, J. Cleaner Prod. 186 (2018) 933–942, https://doi.org/10.1016/j.jclepro.2018.02.138.